Spectroscopic study of partially oxidized BN nanoscrolls induced by low frequency ultrasonic irradiation

Rany Miranti[a], Muhammad Saqib Qayyum[a], Anuvansh Sharma[a],
Mari-Ann Einarsrud[a], Narcis Mestres[b], Maria Benelmekki[a,c*]

[a] *Department of Materials Science and Engineering, NTNU Norwegian University of Science and Technology, Sem Saelands vei 12, 7491 Trondheim, Norway*

[b] *Institut of Material Science of Barcelona (ICMAB-CSIC), Campus de la UAB, 08193 Bellaterra, Barcelona, Spain*

[c] *College of Engineering, Swansea University, Bay campus, Fabian Way, Swansea, UK*

corresponding author: maria.benelmekki@swansea.ac.uk

Abstract

In comparison to carbon nanostructures, hexagonal boron nitride (hBN) nanostructures show better biocompatibility and lower cytotoxicity. However, research studies on hBN nanostructures for biomedical applications are still in an early stage, which limits the current knowledge about this group of materials, particularly their functionalization. Herein, we report a simple and scalable two-step method for the simultaneous synthesis and functionalization of hBN nanosheets (NSHs) and nanoscrolls (NSCs). The first step is conventional chemical exfoliation under alkaline conditions to weaken the interlayer interactions. The second step is exposure to low-frequency ultrasonic irradiation to obtain partially oxidized NSHs and NSCs. The successful formation of both NSHs and NSCs is confirmed using electron microscopy. The effective incorporation of O atoms into hBN nanostructures was confirmed through i) the changes in the optical bandgaps deduced from UV-vis absorption, and ii) the decrease in B atoms bonded to three N atoms and the increase in the BN_xO_y component observed using high-resolution XPS.

Raman spectroscopy was used to analyze the evolution of the active phonon modes upon further exposure to irradiation, and showed a phase transition from sp^2 to a mixture of sp^2–sp^3 bondings at the occurrence of the shape transformation from NSHs to NSCs.

1. Introduction

Graphene and hexagonal boron nitride (hBN) monolayers have been in the research spotlight since the discoveries of their fascinating properties, such as high mechanical strength, transparency, good thermal conductivity as well as excellent chemical and thermal stability. Both materials have attracted significant interests in biological applications such as tumor labeling, sensing and targeting [1]. However, carbon-based nanomaterials show higher toxicity in both in-vivo and in-vitro investigations. BN nanostructures, instead, seem to have better biocompatibility and lower cytotoxicity than carbon nanostructures [1].

Two-dimensional hBN nanosheets (hereafter NSHs) show higher performance than their bulk counterpart which is appealing for both fundamental science and commercial applications. However, currently, the conventional methods to prepare nanostructures from their bulk counterpart are ineffective and might require appropriate solvents, which are usually expensive and need special care during handling [2, 3]. On the other hand, the synthesis of one-dimensional hBN nanostructures, such as nanotubes, is still under intensive research, and almost all the available information related to these nanostructures is based on theoretical and simulation works [1].

On the other hand, besides the technological advantages offered by nanotubes, nanoscrolls (hereafter NSCs) offer additional advantages due to their open tubular structures, which makes the access to their inside a relatively easier task. Moreover, NSHs can be functionalized, and molecules can be attached to their surface prior to their rolling-up to form NSCs; so that they can be used in controlled biomedical applications such as drug delivery systems [4].

Research studies on BN nanostructures for biological and biomedical applications have only been conducted over the past few years, so that knowledge on this group of materials and particularly their functionalization for different purposes is still limited. It is proven that many novel properties can emerge from a material through functionalization. For this reason, the functionalization of hBN layers is a major topic in materials science. Particularly, the properties of hBN can be tailored and new features and applications can be created directly via functionalization. However, the high chemical stability and inertness of hBN hinder its surface modification, making the functionalization challenging [1, 5]. To date, different functional groups such as hydroxyl, amino, ether, and amine groups, among others, have been incorporated into hBN structures through chemical functionalization. The hydroxyl group functionalization is the most suitable for hBN, as the OH groups act as anchoring points for further reactions towards many complex BN derivatives, for a wide range of applications such as biological processes [1, 4].

Recent work on hydroxylation of hBN has focused on acquiring hBN NSHs by chemically exfoliating bulk hBN powder. Lee *et al.* reported the exfoliation and functionalization of hBN by ball milling in an aqueous NaOH solution [6]. The

hydroxide-assisted ball milling enhanced the yield and dispersibility of hBN. The use of an aqueous NaOH solution to provide inserted Na ions were further developed by Fu *et al*. [7]. In their work, hBN particles were dispersed in a NaOH solution and exposed to a pulsed ultrasound resulting in increased yield of hBN NSHs [7]. The exfoliation and self-curling of hBN NSHs were also investigated by Li *et al*. [3], where they developed a low-temperature process to exfoliate hBN and produce NHSs, by heating a mixture of hBN powder, KOH and NaOH in a Teflon-lined autoclave at 180 °C for 2 h [3].

In this work, we present a simple and scalable two-step method for the simultaneous formation and functionalization of hBN NSHs and NSCs. The first step is conventional chemical exfoliation under alkaline conditions, and the second step is exposure to low-frequency ultrasonic irradiation. The successful formation of NSHs and NSCs was confirmed using scanning electron microscopy (SEM) and transmission electron microscopy (TEM). The effective incorporation of O atoms to hBN nanostructures was confirmed using a combination of spectroscopic techniques. UV-vis spectra were used to illustrate the changes in the optical bandgaps, whereas X-ray photoelectron spectroscopy (XPS) was used to study the chemical composition and electronic states of the different components under ultrasonic irradiation. In addition, the hBN NSHs undergo a phase transition from sp^2 bonding to a mixture of sp^2 and sp^3 bonding under ultrasonic irradiation. This transformation was identified using Raman spectroscopy by analyzing the evolution of the active phonon modes upon exposure to irradiation. This phase transition is attributed to the asymmetric vibrations and bending deformations of hBN NSHs upon scrolling to form NSCs.

2. Experimental

2.1. Materials and methods:

hBN powders with maximum particle size of ~ 10 μm manufactured by Goodfellow Cambridge Limited (99.5% purity), potassium hydroxide (KOH) pellets (ACS Reagent), sodium hydroxide (NaOH) pellets (ACS Reagent), and ion exchange resin (Amberlyst - 15-hydrogen form) were purchased from Sigma Aldrich. All chemicals were used as received. The exfoliation was performed by mixing NaOH (2.060 g), KOH (2.740 g) and hBN powders (1.0 g) and heating in a PTFE lined stainless steel autoclave at 200 °C for 3 h. After cooling to room temperature, the sample was washed with deionized water and ethanol several times. The solution was centrifuged and treated with ion exchange resin to achieve a pH of 6.7. The resulting aqueous dispersion was sonicated for 30 min using a 5.5" cup-horn sonicator (QSonica Q700) with a water-cooling system at 50% maximum amplitude.
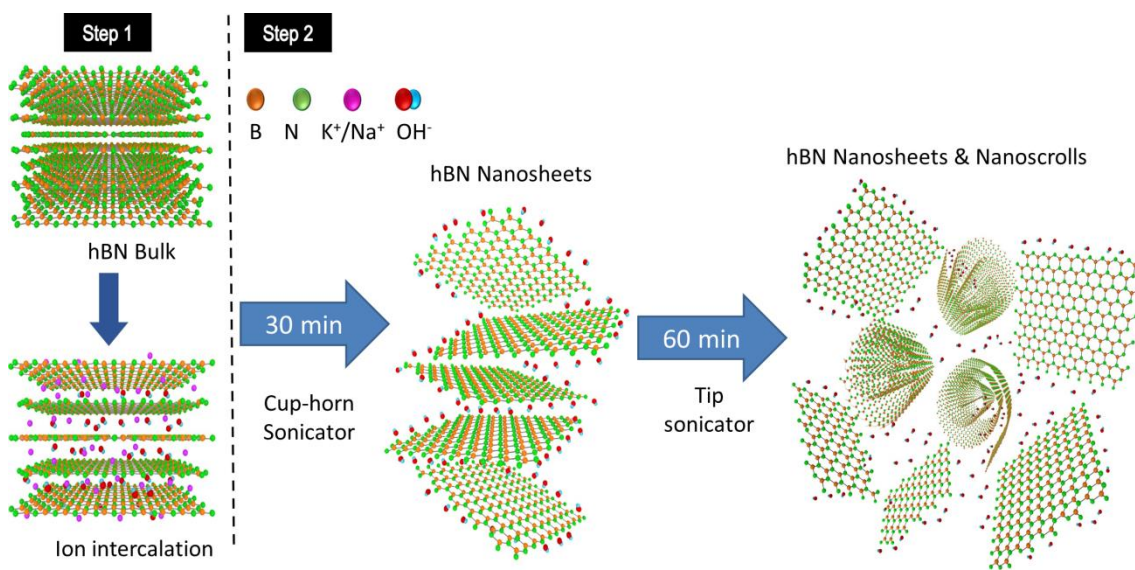

Figure 1: Schematics of the two-step synthesis process employed for the simultaneous

exfoliation and functionalization of the hBN nanostructures. During step 1, the chemical exfoliation of the BN NSHs under molten alkaline conditions is achieved. In step 2, the sample is subjected to low frequency ultrasonic irradiation to obtain partially oxidized NSHs and NSCs.

The dispersion was centrifuged at 3500 rpm and the supernatant was collected as sample S1. Part of the supernatant was further sonicated at 20 kHz generated by a commercial 1/4" tip-sonicator (QSonica - Q700) at 50% of maximum amplitude for another 60 min resulting in a calorimetric power density of ~ 25 W and the supernatant collected was sample S2. For this study, the pristine hBN particles were used as a reference (sample S0). Schematic of the synthesis process is provided in figure 1.

2.2. Characterization:

SEM imaging was performed using a Hitachi S-5500 in-lens cold field emission electron system, at an accelerating voltage of 5 kV. Raman spectra were performed using Renishaw micro-confocal Raman microscope system at room temperature with an excitation wavelength of 532 nm. X-ray photoelectron spectroscopy (XPS) analysis was performed with a Kratos Axis UltraDLD 39-306 electron spectrometer equipped with a monochromated AlKa source operated at 150 W. All the spectra were corrected to carbon peak (C1s at 284.5 eV) and the data were analyzed using CasaXPS processing software. Samples for SEM imaging, Raman spectroscopy, and XPS measurements were dropped onto SiO_2/Si substrates and stored to dry at room temperature in clean-room. TEM analyses were performed on Jeol JEM 2100 microscope operated at 200 kV. A small amount of the sample suspension was dripped using a micropipette on a TEM grid and left to dry on a filter paper. UV-vis analyses were performed using a Thermo Scientific Evolution 220 UV-Visible spectrophotometer with an integration time of 0.45 sec and a bandwidth of 2 nm. The sample suspensions were transferred to

cuvettes for UV measurements.

3. Results and discussion

3.1. Preparation of hBN nanostructures

Chemical exfoliations of hBN nanostructures:

In the first chemical exfoliation step of the synthesis process, as reported by Li et al [3], the cations (Na^+ and K^+) firstly absorb on the BN surface inducing a slight curling of the BN surface layers (which may occur on the edges and steps). This behavior allows the insertion of cations (Na^+ or K^+) and anions (OH^-) into the interlayer spaces. Cations are preferably adsorbed on the negatively curved surfaces, while anions are preferably absorbed on positively curved surfaces. When the coverages of K^+, Na^+ and OH^- ions become high enough ($\geq 10\%$) on the two surfaces of a BN monolayer, the self-curling energy can exceed the interlayer binding energy, favoring the peeling-off from the BN bulk [3].
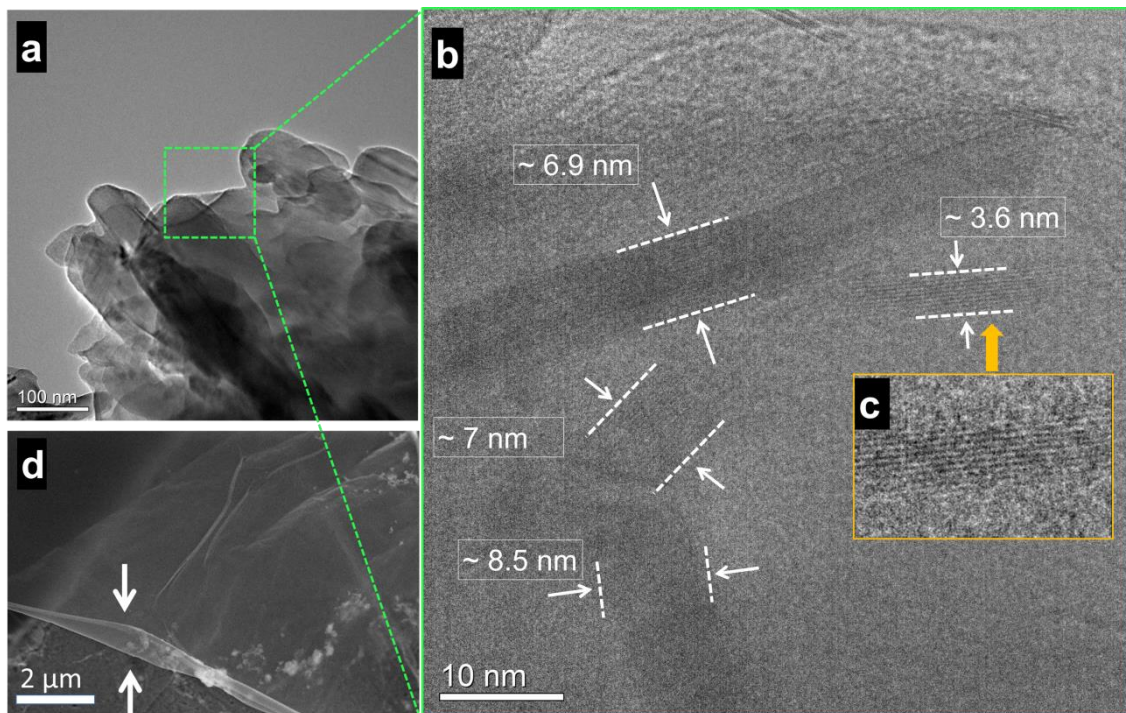
Figure 2: (a) TEM images of an agglomerate of hBN NSHs corresponding to sample S1 (subjected to sonication for 30 min), (b) a magnification of the area indicated in (a) showing the overlap of different NSHs with different orientations, (c) the interatomic distance from the indicated area. (d) SEM image of a single NSH showing the self-curling of the NSH edge, as indicated by the white arrows.

Ultrasonic irradiation exposure:

Figure 2 shows the TEM and SEM images corresponding to sample S1 being subjected to ultrasonic irradiation for 30 min. The TEM image in Figure 2a shows an agglomerate of hBN NSHs. This behavior is expected, as the NSHs tend to form agglomerates to reduce the total surface energy. More SEM images showing the formation and agglomeration of NSHs and the corresponding EDX analysis results are given in figure SI1 and table SI1 of supporting information, respectively. A magnification of the area indicated in Figure 2a shows the overlap of different NSHs with different orientations (Figure 2b). Despite the high transparency of hBN to the electrons (low contrast), it is possible to distinguish the different NSHs. The nanosheet thicknesses vary between ~ 8.5 and ~ 3.6 nm, as indicated in figure 2b. The interatomic distance estimated from image processing using Gatan DigitalMicrograph software (Figure 2c) is in the range 0.334-0.337 nm, corresponding to the distance between two consecutive layers of the edge of an hBN nanosheet [8] (More TEM images and their corresponding FFT patterns are presented in figure SI2 of the supporting information, showing the overlapped NSHs with different orientations). The SEM image in Figure 2d shows a single hBN NSH with an area of ~ 50 μm^2. It is observed that the edge of the NSH is self-curled as indicated with the white arrows.

Figure 3 shows TEM images of sample S2 being sonicated for 30 + 60 min. As shown

in figures 3 a-b, the NSHs are smaller than the ones in sample S1, which can be attributed to their breaking when undergoing prolonged ultrasonic irradiation. On the other hand, the curling-up of the edges of the NSHs is observed. Figure 3c shows a representative NSC of ~ 670 nm of length and ~ 84 nm of outer diameter. Therefore, TEM and SEM analyses clearly show that BN NSHs and NSCs were successfully obtained from the 10 µm hBN particles.
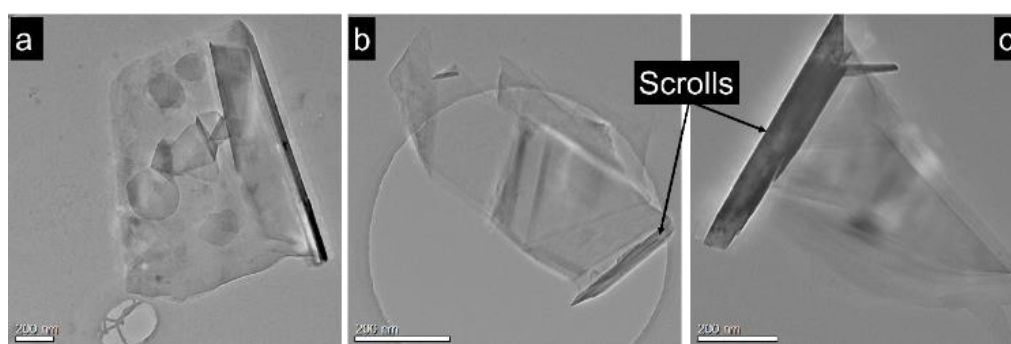

Figure 3: (a) TEM images of hBN NSHs after 90 min ultrasonic irradiation exposition (sample S2), (b) showing the edge scrolling and (c) formation of nanoscroll (NSC).

During the ultrasonic irradiation, the propagation of ultrasonic waves in deionized water, which is used as a medium of dispersion of the NSHs, results in the formation and growth of microbubbles. The ultrasonic energy imparted to the microbubbles lead the activation energy of the hBN NSHs to form NSCs [9]. Although the analysis of SEM and TEM images of sample S1 shows initiation of the scrolling process on the edges of the NSHs, there is no evidence of the formation of full NSCs. Only after the second exposure to ultrasonic irradiation, the formation of NSCs is observed in TEM images (Figure 3c). For a better understanding of the mechanisms involved in the formation of these NSHs and NSCs, UV-vis, Raman, and XPS measurements were performed.

3.2. UV-vis absorption

UV-vis absorption spectra of S0, S1, and S2 were measured (Figure 4a) and the corresponding optical bandgaps (E_g), were analyzed by Tauc's equation:

$$(\omega^2 A = (h\omega - E_g)^2);$$

where A is the optical absorbance, $\omega = 2\pi/\lambda$ is the angular frequency of the incident radiation, and λ the wavelength [10]. Figure 4b shows the optical bandgaps for each sample, estimated from the plot of ($A^{1/2}/\lambda$) versus (λ^{-1}). The values of the bandgaps (E_g) were determined by extrapolating the line intersecting the x axis; where $E_g = hc/\lambda_g$ (λ_g is the wavelength, h is the Planck constant, c is the light velocity). The absorption spectrum of sample S0 shows a pronounced absorption peak at ~ 220 nm, a zero absorption in the visible range (Figure 4a), and a wide indirect bandgap of about 5.2 eV (Figure 4b), in agreement with previously reported data on hBN bulk [6, 11, 12].
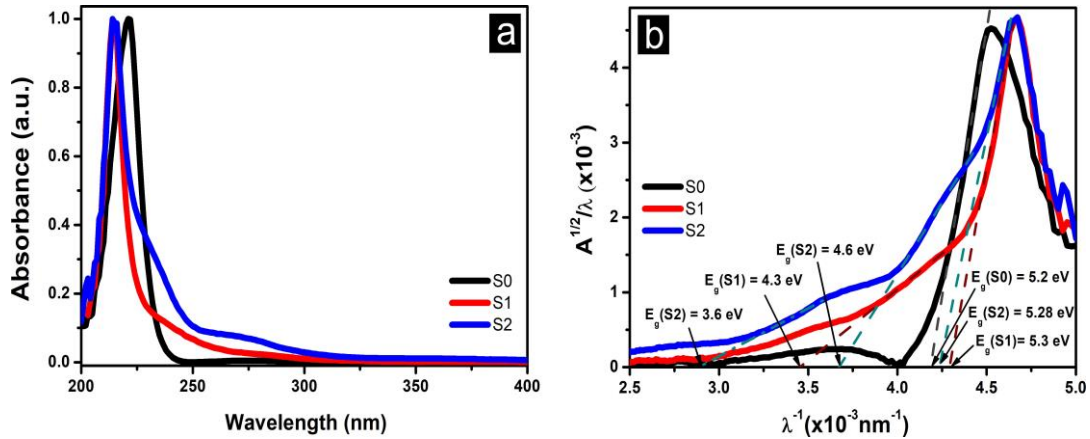

Figure 4: (a) UV-Vis absorption spectra of S0 (black line), S1 (red line) and S2 (blue line). (b) The spectra fitted with Tauc's plot of S0 (black dashed line), S1 (red dashed line), and S2 (blue dashed line).

The sharp absorption peak at ~ 220 nm can be assigned to the intraband transition between the valence band and the conduction band of hBN [13, 14], which is also known to be related to a signature of the BN ring structure in the basal plane [15]. The absorption spectrum of sample S1 shows a blue shift of the pronounced peak from ~ 220 nm to ~ 214 nm, corresponding to an optical bandgap of ~ 5.3 eV. As reported

elsewhere [7, 11, 12], the blue-shift of the absorption peak is an indication of the thickness reduction of the samples from bulk to NSHs, which is in agreement with our SEM and TEM results that show the formation of NSHs (Figures 2 and 3). Moreover, the absorption spectrum of sample S1 shows a weak shoulder at ~ 250 nm, and the corresponding Tauc's plot results in an additional optical bandgap of ~ 4.3 eV. Regarding sample S2, in addition to the blue shift of the main absorption peak from ~ 220 nm to ~ 214 nm, two additional broad shoulders at ~ 235 nm and ~ 275 nm are observed resulting in two additional optical bandgaps of ~ 4.6 eV, and ~ 3.6 eV, respectively (Figure 4b).

These additional optical bandgaps can be related to defects due to functional groups attached to the hBN rings. In fact, previous reports [15] demonstrated that the incorporation of sulfur and oxygen atoms to the hBN NSHs resulted in an additional optical bandgap, indicating changes in the optical and electrical properties of the NSHs. In our case, during ultrasonic irradiation of the samples, cavitation (microbubbles) can lead to the generation of very high local temperatures and pressures in a very short period of time [16]. The energy released from the microbubbles to the hBN nanostructures and to the surrounding medium (water) might induce chemical modification and cleavage of the hBN NSHs, impacting both the surface chemistry and morphology of the NSHs [16]. This is consistent with the TEM analysis, wherein we observed a decrease in the size area of the NSHs together with their scrolling-up (Figures 2 and 3), when increasing the sonification time. On the other hand, ultrasonication might induce splitting of a small percentage of water molecules, and thus providing a source of OH groups [17, 18]. These OH groups react with B atoms in

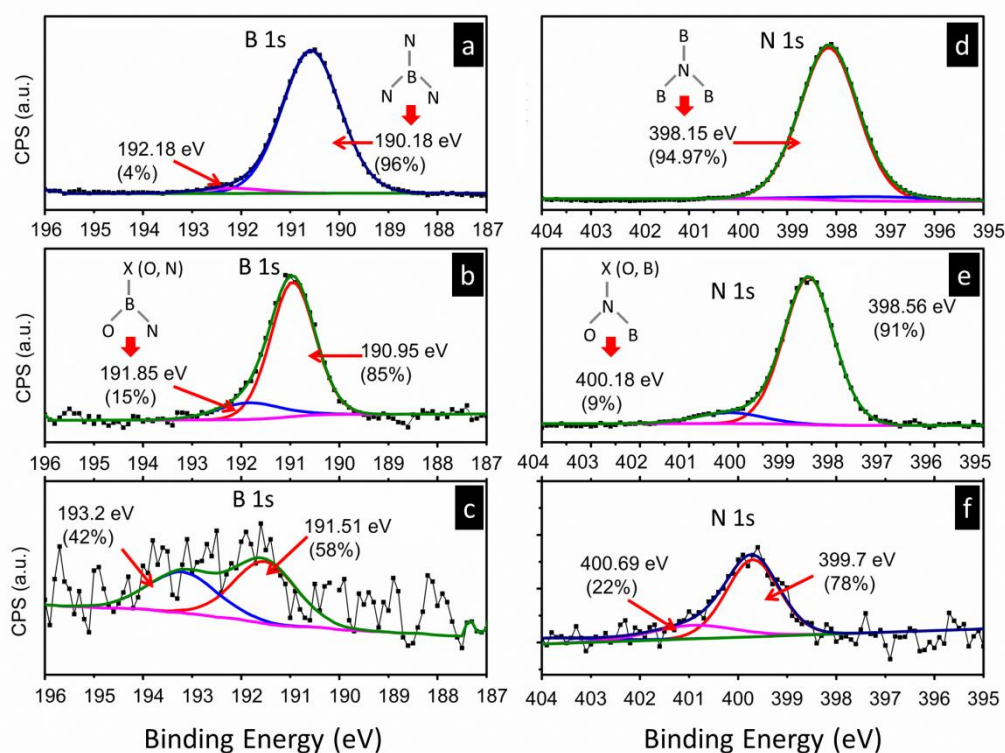the hBN nanostructure owing to the polar covalency of the B-N bonds [1].

Figure 5: XPS spectra and curve fittings for (a, b, c) B1s and (d, e, f) N1s core levels corresponding to (S0, S1, S2), respectively.

3.3. X-ray photoelectron spectroscopy (XPS)

As depicted in figures 5 a and d, the B1s and N1s core level peaks corresponding to sample S0 are located at ~190.18 and ~ 398.15 eV binding energies, respectively, matching reported values for bulk hBN [19]. In addition, the measured atomic percentages show excellent stoichiometry with a B:N ratio of 1.01. The deconvolution of the peak corresponding to B1s at ~ 190.18 eV (Figure 5a) correlated to a B atom

bonded to three N atoms in the typical hBN lattice structure. The second peak at ~ 192.18 eV is correlated to a B atom bonded to one or two N atoms as well as one or two O atoms. Since oxygen has a higher electronegativity than nitrogen, this bonding configuration results in the formation of a peak shifted to higher binding energies. Therefore, this peak indicates that there is a ~ 4% partial bonding of B to O, which can be assigned to a BN_xO_y configuration. On the other hand, analyzing the corresponding N1s core level spectrum, we observe that the peak contains only one component in the main N1s line (Figure 5d) and no signature of N-O bonding is observed. This absence can be attributed to the relatively higher intensity of the N1s peak compared to the B1s peak, as observed in figure SI3-a of supporting information. Therefore, peaks associated with nitrogen and oxygen bonding may be suppressed by the large signal of the N1s peak [19, 20].

Of note, the experimental data in figures c and f (Sample S2) show a higher level of noise corresponding to normalized-signal-to-noise ratios (R_{SN}) of 0.75 in c and 0.88 in f; whereas R_{SN} in figures b and e (Sample S1) are 0.86 and 0.93, respectively (R_{SN} values were obtained using CasaXPS processing software). This behavior is attributed to the small amount of the sample (S2) during data acquisition. In fact when NHSs (sample S1) are exposed to further ultrasonic irradiation (to obtain sample S2), in addition to their scrolling-up, an important decrease in the NSH size occurs (Figures 2, 3, and SI1); and thus, *"nanosize-effects"* become more important. Within this context, the formation of agglomerates is the most plausible mechanism for colloidal nanoparticles (in our case colloidal NHSs and NSCs) to reduce their surface energy [21, 22]. The formed agglomerates remain trapped in the liquid suspension (water). However, after the sample is dropped on the substrate surface and dried, the release of the free-standing

agglomerates from the substrate surface to the surrounding medium is likely to occur, resulting in the unpreventable decrease of the sample amount on the surface of the substrate. Herein, it is important to mention that even if the colloidal nanoparticles are well stabilized and no agglomerates are formed, their release from the dried surface to the surrounding medium might take place in the same way. On the other hand, the distribution of the remaining sample on the surface of the substrate becomes highly inhomogeneous, as confirmed from electron microscopy images. Figure SI4 and Table SI2 show an example of how the amount and the distribution of the sample affect significantly the quality of the acquired data and thus, the accuracy of the analysis results.
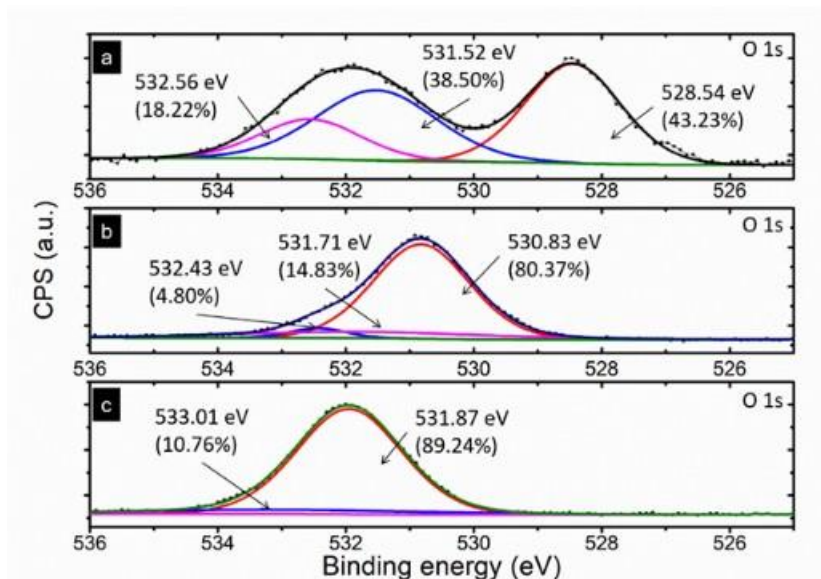

Figure 6: XPS spectra and curve fittings for O1s regions corresponding to (a) S0, (b) S1, and (c) S2 samples.

Figure 5b shows the B1s core level peak, corresponding to sample S1. A shift of the main peak to higher energy (190.95 eV) is observed, in addition to the increase of the

percentage of the B atoms bonded to O from ~ 4% to ~ 15%. Referring to N1s core level spectrum (Figure 5e), in addition to the shift of the N1s main peak from 398.15 eV to 398.56 eV, a new peak at 400.10 eV binding energy appears Indicating the formation of N-O bonding [20]. The percentage of N atoms involved in the bonding to O is ~ 9%. The B:N ratio also decreases from 1.01 (S0) to 0.93 (S1) Indicating changes in the initial stoichiometry of the sample, with a decrease of B atoms bonded to three nitrogen atoms. Moreover, XPS analysis of sample S2 show shifts of the main peaks corresponding to B1s and N1s from 190.95 eV to 191.51 eV, and from 398.56 eV to 399.70 eV, respectively (Figure 5 c, f). In addition, an important increase of the peak area at 400.69 eV associated to N-O bonding is observed, demonstrating the increase of the percentage of N atoms bonded to O from ~ 9% for S1 to ~ 22% for sample S2. The deconvolution of B1s core level peak corresponding to sample S2 (Figure 5c) shows a main peak at 191.51eV (~ 58%) attributed to BN_xO_y, and a second peak at 193.2eV (~ 42%) correlated with the formation of B_2O_3 [20]. The oxygen incorporation may occur during the exposure to ultrasonic irradiation in water resulting in an increase of B-O and N-O bonding, and a decrease of B:N ratio to 0.74 for sample S2. Because the B:N ratio is decreasing, it is unlikely that oxygen atoms are replacing nitrogen atoms as substitutional impurities in the hBN lattice, which indicates that B vacancies are created in the hBN structures, and the O atoms are likely bonding to dangling bonds or defect sites.

The O1s core level peaks samples S0, S1, and S2 are presented in figure 6. Based on the chemical composition of bulk hBN (Sample S0) (figure 5 a and d), only 4% of the total B atoms were bonded to O, predicting that the chemical impurities and surface oxidation of the original powders are likely the origin of the O1s lines observed in

figure 6a). On the other hand, the deconvolution of the O1s peak for sample S1 shows three bonding states of O. The peaks at ~ 530.8 eV (~ 80%) and ~ 531.7 eV (~ 15%) binding energies can be correlated to BN_xO_y, while the peak at ~ 532.4 eV (~ 5%) binding energy can be assigned to B coordinated to three O atoms (hereafter $B(O_3)$) [23].

Figure 6c shows the core level spectrum of O1s region corresponding to sample S2. The deconvolution of the peak results in two peaks located at ~ 531.8 eV (~ 89%), and ~ 533.0 eV (~ 11%) characteristic of BN_xO_y and $B(O_3)$, respectively. Correlating these results with the ones obtained of B1s and N1s in figures 5 c and f, we speculate that the prolonged exposure to the ultrasonic irradiation enhances the selective bonding of OH groups to B sites, and thus, more O atoms are incorporated to the structure. This enhanced incorporation of OH groups leads to NSHs with higher defect concentration on B sites resulting in optical changes, as confirmed from the UV-visible study.

3.4. Raman spectroscopy

Raman spectra of samples S0, S1, and S2 are shown in figure 7a. For sample S0, the Raman spectrum exhibits an intense phonon peak at 1365 cm^{-1} with a full width at half maximum (FWHM) of approximately 10 cm^{-1}. As the symmetry group analysis shows that bulk hBN has a hexagonal symmetry (D6h) that belongs to the P63/mmc symmetry group with one Raman active mode at high frequency (E_{2g} symmetry) [24, 25], we assign the peak at 1365 cm^{-1} to E_{2g} symmetry of the BN in-plane modes, which is correlated to the sp^2-bonded BN [24, 26].

The chemical exfoliation and exposure to ultrasonic irradiation result in a blue shift of the E_{2g} phonon modes of both sample S1 and S2, as depicted in the inset of Fig. 7a. The peak shift in sample S1 is approximately 3 cm^{-1} followed by a notable decrease in the

peak intensity and no broadening of the peak is observed. Previous works reported a simultaneous blue shift and a decrease in the intensity of the phonon modes caused by a decrease in the number of hBN layers [27]. The detected shift of the Raman peak frequency of approximately 3 cm^{-1} in sample S1 is induced by the in-plane compressive stress, leading to the shortening of the B-N bond length in the NSHs [26] and to the weaker interlayer interactions [28]. Thus, the Raman spectrum of sample S1 further confirms the successful peeling-off of the hBN bulk into multilayered NSHs. The Raman shifts of both sample S0 and S1 are well fitted to a single Lorentz function and no additional Raman peak is observed in the Raman spectrum of sample S1, demonstrating that the sample maintains a similar symmetry group as sample S0.
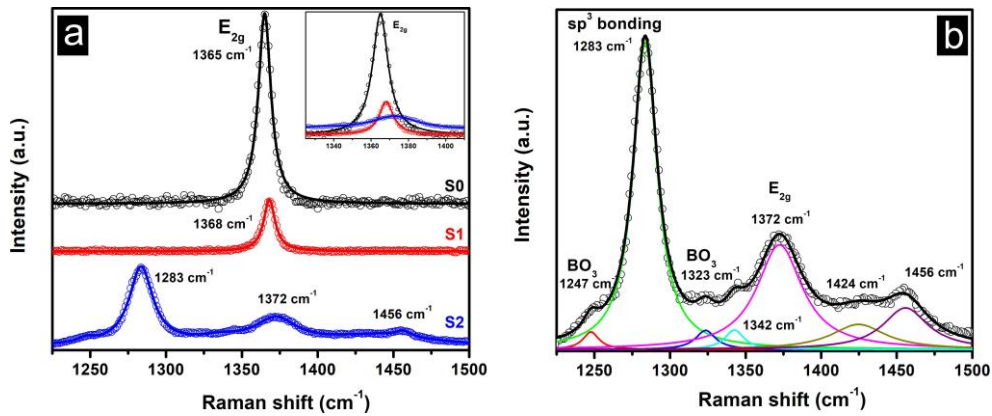

Figure 7: (a) Raman spectrum of S0 (black line), S1 (red line), S2 (blue line). The insert shows E2g mode evolution with increasing sonication time, (b) Raman spectrum of S2 sample fitted with seven Lorentz functions.

The E_{2g} phonon mode for sample S2 is shifted to a higher frequency by approximately 7 cm^{-1} with a notable broadening of the peak achieving a FWHM of ~ 36 cm^{-1}. In addition to the broadening of this peak, new peaks appear, and thus, the spectrum can be fitted to seven Lorentz peaks, as shown in Figure 7b. Of note, the quality of the chemical composition of the samples is not altered during the processing of the samples,

which is confirmed from XPS surveys presented in figure SI3-a of supporting information. Impurities of Na were observed in the three samples, however this Na presence would not affect the Raman spectra. For this reason, we collected more Raman spectra from different areas of sample S1 (figure SI5 of supporting information), and no new phonon modes were observed.

As illustrated in the TEM image (Figure 3c), further exposure to ultrasonic irradiation results in asymmetric rolling up of the NSHs into NSCs. This change from NSHs to NSCs contributes to the broadening of the E_{2g} phonon modes and may be the origin of the appearance of new phonon modes. In addition, the intensity of E_{2g}, correlated to the sp^2 hybridized bonds, decreases during the ultrasound irradiation process, whereas an intense and sharp peak appears at 1283 cm^{-1}. Perim and co-workers performed molecular mechanics and molecular dynamics simulations using the molecular universal force field to address the structural and dynamic aspects of BN NSHs [29]. They suggested that, when the NSHs are rolled-up into NSCs, the layer curvature, torsion, and inversion increase and contribute to the strain energy, and subsequently, the van der Waals interactions of the overlapping surfaces of the rolled layers contribute to the structural stability. Moreover, when the NSHs are rolled-up into NSCs, the B-N bond length and bond angles change and induce weakening of the π-bonds, leading to bond re-hybridization [25, 30], and thus resulting in a mixture of sp^2 and sp^3 hybridization in the NSCs. Therefore, by analogy to the results of hBN nanotubes, and from Raman studies related to the hybridization transition from sp^2 to sp^3 in hBN thin films and nanoparticles [31-34]. To further investigate the origin of the peak at 1289 cm^{-1} and to exclude the possible interference of impurities or contaminants during the synthesis process, additional Raman spectra were collected from different areas of sample S1 in a

wider range from 900 cm^{-1} to 1700 cm^{-1}. As shown in figure SI4 of supporting information, only the active modes corresponding to h-BN nanosheets (E$_{2g}$), and the 2TO mode corresponding to the Si substrate were observed.

The strong peak at 1283 cm^{-1} can be correlated to the presence of sp^3 hybridized BN bonding caused by the asymmetric vibrations and bending deformations of the hBN NSHs. At the current stage of our study, we could not identify the other minor peaks. The peaks at 1247 and 1323 cm^{-1} were previously attributed to vibrations in B(O$_3$) triangles [35], which is consistent with our XPS analysis. Previous reports suggest that the weak peaks around the main peaks are related to the uneven distribution of B or N vacancies owing to substitutional impurities in BN [36]. In our case, for a precise identification of these weak peaks further theoretical and experimental studies are required to understand and correlate both the incorporation of oxygen atoms into BN nanostructures and the rolling up process of these nanostructures.

4. Conclusions

A simple and scalable two-step method for the simultaneous synthesis and functionalization of hBN NSHs and NSCs is presented. The first step consists of conventional chemical exfoliation under alkaline conditions to weaken the interlayer interactions, and the second step is exposure to low-frequency ultrasonic irradiation to obtain partially oxidized NSHs and NSCs:

1) The formations of hBN NSHs with thicknesses varying in the range of 3.6 - 8.5 nm was demonstrated. By increasing the time of exposure to the ultrasonic irradiation from 30 min to 90 min, the NSHs rolled-up to form well-defined NSCs.

2) Spectroscopic studies demonstrated the effective incorporation of O atoms into the structure of NSHs and NSCs. This incorporation was confirmed

through i) the changes in the optical bandgaps, as deduced from UV–vis spectra, ii) the changes in the chemical composition of the nanostructures, deduced from high-resolution XPS study.

3) Raman spectra showed the evolution of the E_{2g} phonon mode, correlated to sp^2 hybridization, and confirmed the formation of NSHs. In addition, the appearance of new active phonon modes (upon further exposure to ultrasonic irradiation), indicated a phase transition from sp^2 bonding to a mixture of sp^2–sp^3 bonding, which is attributed to the asymmetric vibrations and bending deformations of hBN NSHs upon scrolling to form NSCs.

These findings open a new horizon for tunable modification of the morphology and surface chemistry of BN nanostructures for a wide range of applications. Of note, the OH modified BN nanostructures are the most suitable for direct application in various fields such as biological processes, where OH groups serve as initiators for further reactions and designs toward many complex BN derivatives. However, to gain a better understanding of the scrolling mechanism and the incorporation of oxygen to the hBN nanostructures, further experimental, theory, and simulations works are needed to model the underlying mechanisms that determine both the scrolling and the functionalization of hBN nanostructures.

Conflicts of interest

There are no conflicts to declare.

Acknowledgement

References

1. Q. Weng, X. Wang, X. Wang, Y. Bando, D. Golberg, Chem. Soc. Rev. 45 (2016) 3989–4012.

2. L. H. Li, Y. Chen, G. Behan, H. Zhang, M. Petravicc, A . M . Glushenkov, J. Mater. Chem. 21 (2011) 11862–11866.

3. X. Li, X. Hao, M. Zhao, Y. Wu, J. Yang, Y. Tian, G. Qian, Advanced Materials 25 (2013) 2200–2204.

4. J.H. Kim, M. Benelmekki, Two-dimensional nanostructures for biomedical applications, in: M. Benelmekki, A. Erbe (Eds), Frontiers of Nanoscience, Elsevier, 2019, pp 103-120, https://doi.org/10.1016/B978-0-08-102572-7.00004-0.

5. A. Pakdel, Y. Bando, D. Golberg, Chem. Soc. Rev. 43 (2014) 934–959.

6. D. Lee, B. Lee, K. H. Park, H. J. Ryu, S. Jeon, S. H. Hong, Nano Letters 15 (2015) 1238–1244.

7. L. Fu, G. Chen, N. Jiang, J. Yu, C.-t. Lin, A. Yu, J. Mater. Chem. A 4 (2016) 19107–19115.

8. M. Sajjad, W. M. Jadwisienczak, P. Feng, Nanoscale 6 (2014) 4577–4582.

9. C. A. Amadei, I. Y. Stein, G. J. Silverberg, B. L. Wardle, C. D. Vecitis, Nanoscale 8 (2016) 6783–6791.

10. J. Tauc, R. Grigorovici, A. Vancu , Phys. Stat. Sol. 15 (1966) 627–37.

11. Y. Liao, K. Tu, X. Han, L. Hu, J. W. Connell, Z. Chen, Y. Lin, Scientific Reports 5

(2015) 14510.

12. L. Song, L. Ci, H. Lu, P. B. Sorokin, C. Jin, J. Ni, A. G. Kvashnin, D. G. Kvashnin, J. Lou, B. I. Yakobson, P. M. Ajayan, Nano Letters 10 (2010) 3209–3215.

13. R. Schuster, C. Habenicht, M. Ahmad, M. Knupfer, B. Büchner, Phys. Rev. B. 97 (2018) 041201.

14. R. Sevak Singh, R. Yingjie Tay, W. Leong Chow, S. Hon Tsang, G. Mallic, E. H. Tong Teo, Appl. Phys. Lett. 104 (2014) 163101.

15. G. R. Bhimanapati, D. Kozuch, J. A. Robinson, Nanoscale 6 (2014) 11671–11675.

16. K. S. Suslick, Sonochemistry, Science 247 (1990) 1439-1445.

17. J. E. Funk, International Journal of Hydrogen Energy 26 (2001) 185–190.

18. K. Wark , Thermodynamics, 6th ed., McGraw-Hill Inc., US, 1998.

19. J. F. Moulder, Handbook of X-ray Photoelectron Spectroscopy: A Reference Book of Standard Spectra for Identification and Interpretation of XPS Data, Physical Electronics Division, Perkin-Elmer Corporation, 1992.

20. C. Guimon, D. Gonbeau, G. Pfister-Guillouzo, O. Dugne, A. Guette, R. Naslain, M. Lahaye, Surf. Interface Anal. 16 (1990) 440– 445.

21. G. Cao, Y. Wang, Nanostructures and nanomaterials, 2nd ed., World Scientific publishing , 2011.

22. M. Benelmekki, Nanomaterials: the original product of nanotechnology, IOP Concise physics, Morgan & Claypool publishing , 2019.

23. D. Schild, S. Ulrich, J. Ye, M. Stüber, Sol. Stat. Sci. 12 (2010) 1903–1906.

24. Q. Huang, D. Yu, Z. Zhao, S. Fu, M. Xiong, Q. Wang, Y. Gao, K. Luo, J. He, Y. Tian, J. Appl. Phys. 112 (2012) 053518.

25. L. Wirtz, A. Rubio, Optical and Vibrational Properties of Boron Nitride Nanotubes, in: Optical and Vibrational Properties of Boron Nitride Nanotubes, volume 6, Springer, New York, NY, 2009, pp. 341–348.

26. R. Arenal, A. C. Ferrari, S. Reich, L. Wirtz, J.-Y. Mevellec, S. Lefrant, A. Rubio, A. Loiseau, Nano Letters 6 (2006) 1812–1816.

27. R. V. Gorbachev, I. Riaz, R. R. Nair, R. Jalil, L. Britnell, B. D. Belle, E. W. Hill, K. S. Novoselov, K. Watanabe, T. Taniguchi, A. K. Geim, P. Blake, Small 7 (2011) 465–468.

28. W. Zhu, X. Gao, Q. Li, H. Li, Y. Chao, M. Li, S. M. Mahurin, H. Li, H. Zhu, S. Dai, Angewandte Chem. International Ed. 55 (2016) 10766–10770.

29. E. Perim, D. S. Galvao, Nanotechnol. 20 (2009) 335702.

30. W. H. Moon, H. J. Hwang, Phys. E: Low-dimensional Syst. and Nanostruct. 23 (2004) 26–30.

31. P. M. Ossi, A. Miotello, Appl. Organomet. Chem. 15 (2001) 430–434.

32. T. Werninghaus, J. Hahn, F. Richter, D. R. T. Zahn, Appl. Phys. Lett. 70 (1997) 958–960.

33. M. Benelmekki, M.A. Djouadi, E. Guiot, V. Mortet, N. Mestres, and G. Nouet, , Surf. Coat. Technol. 116-119 (1999) 93-99.

34. J. Lu, Q. Ren, L. Sun, J. Yu, Y. Chen, X. Shen and Z. Chen, Appl. Phys. Express 7 (2014) 022401-1 DOI:10.7567/APEX.7.022401.

35. S. V. Stefanovsky, K. M. Fox, J. C. Marra, Materials Research Society

Symposium Proceedings 1518 (2013) 53–58.

36. S. Feng, L. Hou, X. Liu, Y. Gao, X. Li, Q. Wang, Z. Chen, G. Jia, J. Zheng, Applied Surface Science 285 (2013) 817–822.